

Carbon Nanotube-Based 100s TeV/m-Level Particle Accelerators Driven by High-density Electron Beams

Bifeng Lei,^{1,2,*} Hao Zhang,^{1,2} Cristian Bontoiu,^{1,2} Alexandre Bonatto,³
Javier Resta-López,⁴ Guoxing Xia,^{5,2} Bin Qiao,⁶ and Carsten Welsch^{1,2}

¹*Department of Physics, The University of Liverpool, Liverpool, L69 3BX, United Kingdom*

²*Cockcroft Institute, Warrington WA4 4AD, United Kingdom*

³*Federal University of Health Sciences of Porto Alegre, Porto Alegre, RS, 90050-170, Brazil*

⁴*ICMUV, Universidad de Valencia, 46071 Valencia, Spain*

⁵*Department of Physics and Astronomy, The University
of Manchester, Manchester M13 9PL, United Kingdom*

⁶*Center for Applied Physics and Technology, HEDPS, and SKLNPT,
School of Physics, Peking University, Beijing 100871, China*

(Dated: February 21, 2025)

Abstract

Solid-state materials, such as carbon nanotubes (CNTs), have the potential to support ultra-high accelerating fields in the TV/m range for charged particle acceleration. In this study, we explore the feasibility of using nanostructured CNTs forest to develop plasma-based accelerators at the 100s TeV-level, driven by high-density, ultra-relativistic electron beams, using fully three-dimensional particle-in-cell simulations. Two different acceleration mechanisms are proposed and investigated: the surface plasmon leakage field and the bubble wakefield. The leakage field, driven by a relatively low-density beam, can achieve an acceleration field up to TV/m, capable of accelerating both electron and positron beams. In particular, due to the direct acceleration by the driving beam, the positron acceleration is highly efficient with an average acceleration gradient of 2.3 TeV/m. In contrast, the bubble wakefield mechanism allows significantly higher acceleration fields, e.g. beyond 400 TV/m, with a much higher energy transfer efficiency of 66.7%. In principle, electrons can be accelerated to PeV energies over distances of several meters. If the beam density is sufficiently high, the CNT target will be completely blown out, where no accelerating field is generated. Its threshold has been estimated. Two major challenges in these schemes are recognised and investigated. Leveraging the ultra-high energy and charge pumping rate of the driving beam, the nanostructured CNTs also offer significant potential for a wide range of advanced applications. This work represents a promising avenue for the development of ultra-compact, high-energy particle accelerators. We also outline conceptual experiments using currently available facilities, demonstrating that this approach is experimentally accessible.

I. INTRODUCTION

The development of ultra-compact plasma-based particle accelerators is primarily beneficial from the ultra-high acceleration gradient, which is achieved through coherent plasma wave excitation driven by high-intensity beams, such as photon or charged particle beams. The acceleration field in plasma wave is dependent upon the plasma density as $E = m_e c \omega_p / e \simeq 9.6 \sqrt{n_e [10^{22} \text{cm}^{-3}]} \text{ [TV/m]} \propto n_e^{1/2}$ where n_e is the ambient plasma electron density, and m_e and c are rest electron mass and speed of light in vacuum respectively, and

* bifeng.lei@liverpool.ac.uk

$\omega_p = \sqrt{4\pi e^2 n_e / m_e}$ is the plasma frequency [1]. The current state-of-the-art gaseous plasma-based accelerators, for example, laser-driven wakefield accelerator (LWFA) or beam-driven wakefield accelerator (PWFA), practically work with the low-density classical plasma in the range of $n_e \sim 10^{14-18} \text{cm}^{-3}$. This density can, in principle, support an acceleration gradient of approximately $G \sim 1 - 100 \text{ GeV/m}$ [2–5].

To achieve a higher G , denser plasma is required, which, for example, naturally exists in metallic crystals. The density of charge carriers (conduction electrons) in these crystals ranges from $10^{20-24} \text{cm}^{-3}$. These conduction electrons are quantum degenerate at low temperatures (e.g., room temperature), forming a degenerated Fermi electron gas that is collisionless with the ionic lattice and dominated by collective and coherent effects [6]. The coherent plasma oscillation of these conduction electrons, referred as plasmon, can be excited by external sources, e.g. photons or fast electron beams [7]. With a high-intensity beam driver, the plasmon amplitude can be extremely high, in the order of TV/m. Such intense fields could be used for the charged particle acceleration [8–10]. However, the solid-density plasma wakefield acceleration using natural crystals remains unrealisable due to the limitation of angstrom-size channels and the unavailability of suitable drivers, e.g. high-intensity x-ray lasers [11, 12].

In recent years, the advent of modern nanofabrication techniques has enabled the fabrication of nanostructures and metamaterials with enhanced flexibility in parameters such as structure, density, and thickness compared to their unstructured crystalline counterparts, achieved through the controlled deposition of porous materials [13, 14]. Recent numerical simulations have demonstrated that pure graphene layers of plasma density 10^{22}cm^{-3} can achieve a 4.79 TeV/m acceleration gradient for electron acceleration by utilising a high-intensity, 10^{21} W/cm^2 , ultra-violet laser to drive plasma wakefield [15]. Nevertheless, the preparation of such laser pulses is still a challenging process [16, 17].

A carbon nanotube (CNT) is a graphene-based single- or multi-wall tubular structure. With a typical inner diameter of a few nm and a length of up to mm, CNTs exhibit excellent mechanical, thermodynamic and electronic properties [18, 19]. Depending on their chirality, CNTs can be metals (armchair) which can provide wall plasma densities in the range of $10^{22-24} \text{cm}^{-3}$ with a vacuum hollow channel permitting the channelling of optical laser pulses or particle beams over extended distances to excite the strong plasmons on the wall surface, referred as surface plasmons (SPs) [20–23]. However, at the current stage, it is also

not feasible to directly employ these CNTs for particle acceleration due to the inability to resonantly match the μm dimensions of available photon or particle beams with a few nm natural dimensions of CNTs.

Nanostructured CNT targets, e.g. porous or bundled CNT as shown in Fig. 1, arranged as CNT arrays or forest, offer a greater degree of flexibility in geometric structure, density, and surface structures than unstructured solids [24–26]. This is due to the unique characteristics of CNT arrays, which can be tailored more specifically through controlled synthesis and manipulation of their structural and compositional properties. The wall density being adjusted to a range of $n_t \sim 10^{19-24}\text{cm}^{-3}$ can facilitate a 0.1 – 100 TV/m-level accelerating and focusing field. The diameter of the vacuum hollow can range from hundreds of nm to a few μm , enabling the channelling of either a photon beam (such as an optical laser pulse) or a high-energy charged particle beam for a sufficient length of time to drive solid-state surface plasmon while simultaneously mitigating adverse effects, e.g. collision [27], beam filamentation [28], bulk radiation [29], etc. As no damage has been observed experimentally yet in these crystal samples by interacting with an ultra-short electron beam due to the relativistic plasmonic effects [30], this CNT target may support collisionless solid-density plasmas. In modern laboratories, porous CNT targets can be prepared using the so-called anodic aluminium oxide (AAO) template method, which provides excellent tunability through control of the AAO template’s pore texture [31–33]. Moreover, the preparation of CNT bundle targets can be achieved through several methods, e.g. chemical vapour deposition (CVD), arc discharge or template-assisted growth. Each of these methods offers a distinct level of control over the properties of the resulting CNTs and their bundles [34–37].

Coherent oscillations of the conduction electron gas in the these nanostructured CNTs can be excited when an ultra-relativistic, high-density electron beam (referred as the driving beam) passes through the vacuum channel (see Fig. 1). During this process, conduction electrons within the CNT walls are radially compressed and gain transverse momentum. The key distinction between nanostructured CNT-based plasma and the uniform plasma typically used in LWFA and PWFA experiments lies in the inner and outer surfaces of these hollow targets, as depicted in Fig. 1(d). The conduction electrons may be trapped inside the CNT wall by potential barriers (vertical curve) formed across these surfaces, leading to unique electron dynamics. Whether the electrons can cross these surfaces determines the excitation of SPs.

When the driving beam density is moderate, the compressed electrons may rebound due to the space charge force. If their inward momentum is sufficient to overcome the potential barrier on the inner surface, the electrons can be emitted into the vacuum region, generating a strong electrostatic field on the order of TV/m, suitable for particle acceleration [38]. Here, an individual conduction electron moves freely as being in the uniform plasma and can generate the plasma wave or plasma bubble wakefield in the vacuum channel. Using an effective density model [38], the field amplitude of the bubble wakefield has been theoretically predicted to approach the coherence limit of collective fields as $E_{wb} \simeq m_e c \omega_p / e$. This limit, also known as cold relativistic wakefield breaking field [1], is significantly higher than the amplitude of SP [22] and exceeds the lattice ionic field, where polaritons play a negligible role in the acceleration process [39]. Conversely, if the driving beam density is low and the conduction electrons lack sufficient momentum to overcome the potential barrier, they accumulate periodically on the inner surface, forming conventional SPs. In cases where the CNT wall has a finite thickness and the driving beam density is extremely high, conduction electrons may acquire enough outward momentum to escape from the outer surface, leading to their full ejection from the CNT structure. We define this phenomenon as blowout.

In this paper, we present a 100s TeV/m-level plasma accelerator by channelling an ultra-relativistic electron beam through CNT targets such as those shown in Fig. 1. Two key acceleration mechanisms are demonstrated: leakage field (Sec. III) and bubble wakefield (Sec. IV). We demonstrate for the first time that the electromagnetic (EM) fields generated by SPs can penetrate deeply from the inner surface into the vacuum region, referred here to as the leakage field, providing a sub-TV/m-level automatically phase matched accelerating and focusing field for both electron and positron beams. This mechanism can be driven by a low-density electron beam and is feasible with currently available experimental facilities. We further demonstrate that with a moderately intensity driving beam, the conduction electrons can freely cross the inner surface and form the bubble wakefield inside the vacuum channel. The amplitude of this electrostatic field can reach several hundreds TV/m, which is remarkably an order of magnitude higher than the coherence limit predicted by previous models using an effective uniform density wall [38]. This significant increase in field strength is attributed to the suppression of plasma wave breaking. An ultrashort electron beam with nC-level charge can be self-trapped and accelerated to several GeV over distances as short as 100 μm , achieving an ultra-high acceleration gradient of about 73.0 TeV/m and a high

energy transfer efficiency of 67%, as shown in our simulations (Seen in Sec. IV). The longitudinal acceleration field inside the vacuum channel is radially uniform and can lead to the conservation of the energy spectrum of the witness beam. Another notable feature is that the transverse focusing field vanishes within the vacuum region but reaches 10^8 TV/m-level amplitudes within the CNT walls. This ensures that the quality of the accelerated electron beam is maintained and also suggests the potential for accelerating positively charged particles. We also show that this CNT-based acceleration is dynamically stable and can be efficiently scaled with n_b/n_t , where n_b is the driving beam density. Additionally, this configuration minimises radiation reaction effects, as most of the accelerated particles remain confined within the vacuum channel. This makes such systems highly promising for future high-energy applications, with their proven ability to sustain extreme fields.

II. GEOMETRY OF NANOSTRUCTURED CNT TARGETS AND NUMERICAL SIMULATION

The schematic geometry of the nanostructured CNT targets, fabricated by arranging CNT wires into specific array patterns such as porous and bundled configurations, is illustrated in Fig. 1 (a) and (b), respectively. Fully 3D particle-in-cell (PIC) simulations were performed using the code WarpX [40] to model these structures. The transverse layout of the targets is shown in Fig. 1(c), where the distribution patterns of the bundles or pores are initialised with diameter d in the PIC simulations as centralised virtual layers around the central axis. These layers are characterised by a filling factor, f_f , which describes the occupation of each layer by bundles or pores, and a gap, g , between adjacent layers. For a CNT bundled target, as shown in Fig. 1, the black spots represent the CNT bundles with a density of n_t , which is made of hundreds of CNT wires, while the remaining areas are vacuum. For a CNT porous target, the black spots represent the vacuum pores, and the surrounding areas are made of CNT wires with the same density, n_t . For both cases, a vacuum channel with a radius r_t of a few μm radius r_t is created at the centre to guide the driving beam. This set of parameters controls the effective plasma density, which will, in turn, guide the target design in possible future proof-of-principle experiments. For instance, the effective density of a CNT bundled

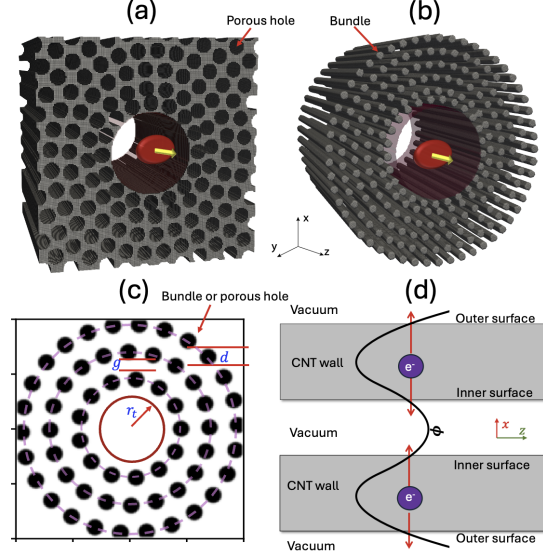


Figure 1. Schematic illustration of (a) porous and (b) bundle CNT targets, arranged in the form of CNT arrays. The boundary of the vacuum channel is indicated by the light red surface surrounding the axis, while the driving beam is represented by the red spots with propagation direction indicated by yellow arrows. Each bundle or the porous wall could be composed of hundreds of single-walled or multi-walled carbon nanotubes. (c) Transverse layout of structured CNT target implemented in simulations. The black spots indicate the locations of CNT bundles or pores which occupy each centralised virtual layer by a filling factor f_f . The red circle indicates the position of the inner surface. (d) A slice of nanostructured CNT target. The conduction electrons (purple spots) have the probability to transit across the inner and outer surfaces. The black curve represents the transverse potential profile.

target can be estimated by

$$n_{\text{bundle,eff}} = n_t \frac{N f_f}{1 + (N - 1)(1 + g/d)}, \quad (1)$$

and for a CNT porous target, it is

$$n_{\text{porous,eff}} = n_t - n_{\text{bundle,eff}}, \quad (2)$$

where N is the number of layers. In the simulations, seven layers are configured with $f_f = 0.65$. Unless declared, the initial bundle density is set to $n_t = 2 \times 10^{22} \text{ cm}^{-3}$ which gives the cold plasma wavelength $\lambda_{pe} = 0.23 \mu\text{m}$. The diameter of a bundle or porous hole is $d = 200 \text{ nm}$ with $g = 70 \text{ nm}$ gap between each virtual layer. The radius of the vacuum core is

$r_t = 0.75 \mu\text{m}$. As a result, the effective wall density of bundle and porous targets are equal, given by $n_{\text{eff}} = n_{\text{bundle, eff}} = n_{\text{porous, eff}} = 1 \times 10^{22} \text{ cm}^{-3}$. From here on, we use n_{eff} to denote the effective plasma density of either porous or bundle CNT wall. Since our simulations show that a porous CNT target supports a more stable acceleration field compared to bundled targets, most of the simulation results in this paper are based on porous CNT targets, unless otherwise specified for cases involving bundled CNT targets.

Since the quantum degeneracy can be calculated as $\chi \simeq 1.5(E_F/k_B T)^{3/2} \simeq 1593.9 \gg 1$ and the correlation as $\Gamma \simeq 0.54n_t^{1/3}a_0^{-1} \simeq 12.2 \gg 1$ at room temperature $T = 300 \text{ K}$, the conduction electron plasma in these targets is fully quantum degenerate and correlated. Here, E_F , K_B and a_0 are the Fermi energy, Boltzmann constant and Bohr radius, respectively. As a result, the conduction electrons behave as free electron gas and can be effectively modelled using classical kinetic methods, such as PIC simulations. The coherent wakefield limit is estimated based on the wall density n_t as $E_{wb}(n_t) = m_e c \omega_{pe} / e \simeq 13.5 \text{ TV/m}$, or based on the effective density n_{eff} , $E_{wb}(n_{\text{eff}}) \simeq 9.6 \text{ TV/m}$.

In the simulations, a $3 \mu\text{m}$ -long vacuum region is placed before and after the CNT target to initialise the driving beam and diagnose the emerging accelerated witness electrons, respectively. The species of the targets are carbon atoms, which are set to be singly ionised to generate C^+ ions. The field ionisation is implemented using the ADK method [41]. The dimension of the moving window is $4.8 \mu\text{m} \times 4.8 \mu\text{m} \times 6.4 \mu\text{m}$ with $384 \times 384 \times 512$ cells in x , y , and z directions respectively which gives 16 points in each direction inside each bundle or pores transversely. There are 8 macro particles per cell, which should be sufficient to accurately resolve the electron dynamics inside.

The driving electron beam is characterised by a Gaussian profile with root-mean-square (RMS) dimensions of $\sigma_{r0} = 1.0 \mu\text{m}$ and $\sigma_{z0} = 0.4 \mu\text{m}$ in the transverse and longitudinal directions, respectively, and is represented by 10^7 macro particles in simulations. The beam density is calculated as $n_b = Q_b / [(2\pi)^{3/2} e \sigma_{r0}^2 \sigma_{z0}]$ with Q_b the driving beam charge. The mean initial energy is $1 - 10 \text{ GeV}$, which is significantly higher than the plasmon energy in CNTs, $\hbar\omega_p = 5.4 \text{ eV}$. Such bunches can create hundreds of eV potential over atomic scales, which is sufficient to directly ionise the conduction electrons of carbon atoms in the CNT structure. The ionised electrons can gain kinetic energy far exceeding the Fermi energy [6, 42, 43]. Furthermore, the mean free time of collision between electrons and the lattice vibrations is of the order of ps level, which is much longer than the plasma collective oscillation period at

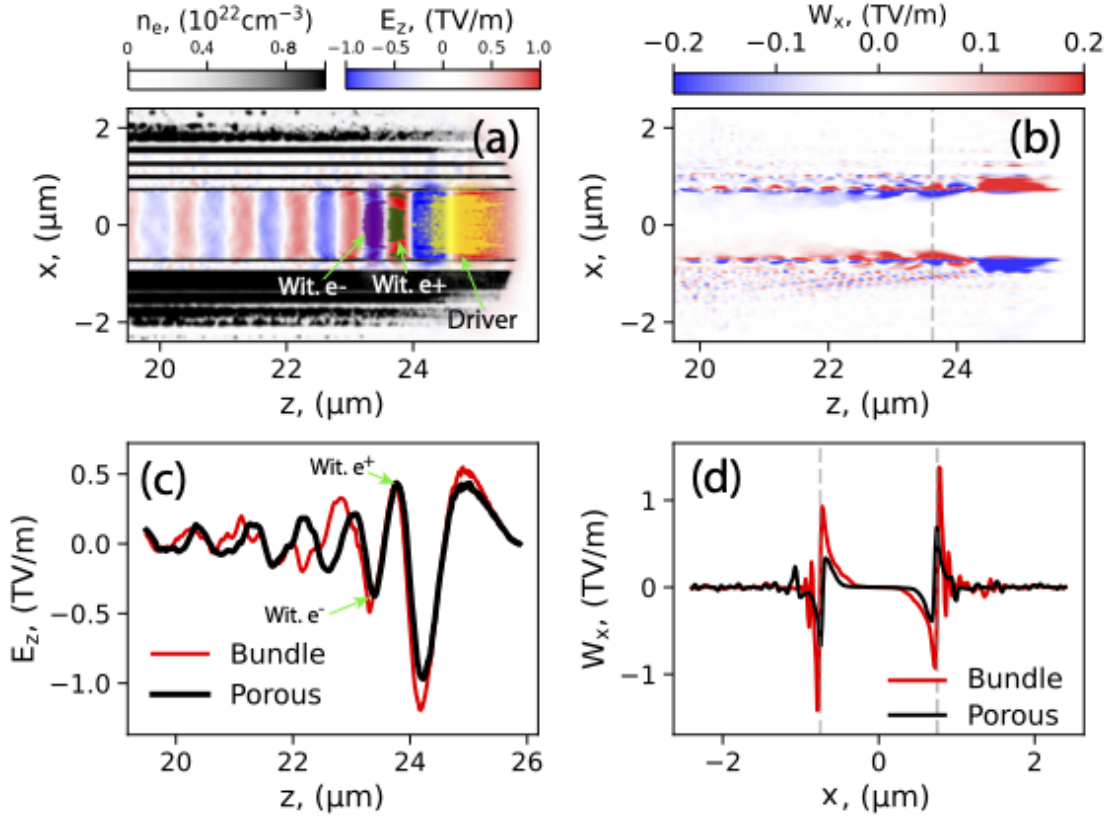


Figure 2. PIC results: Leakage field excitation in nanostructured CNT target. (a) Slice of conduction electron density distribution (grey colourmap), longitudinal electric field E_z (red-blue colourmap), driving and witness electron and positron beams (indicated by yellow, green and purple colors and arrows, respectively). (b) Slice of transverse field W_x along $y = 0 \mu\text{m}$. (c) On-axis ($x = 0$) plot of E_z for porous (black) and bundle (red) targets. (d) Line plot of W_x for porous (black) and bundle (red) targets at $z = 23.5 \mu\text{m}$ indicated by the vertical dashed grey line in (b). The two vertical lines indicate the position of the interface of the CNT wall and vacuum.

the fs-level. Therefore, quantum correction for plasma dispersion, the collision effect and the damping effect on the collective oscillation of the conduction electrons can be neglected [7].

III. SURFACE PLASMON EXCITATION AND LEAKAGE FIELD ACCELERATION

First, we use a 1 GeV driving electron beam with a total charge of $Q_b = 0.3 \text{ nC}$, yielding a beam density of $n_b = 3 \times 10^{20} \text{ cm}^{-3}$, or $n_b/n_t = 0.015$. This beam is unable to drive

the conduction electrons crossing the inner surface, as shown in Fig.2(a), where plasma oscillations remain confined to the surface. However, the electromagnetic field of the SPs can leak into the vacuum region, as shown in Fig.2(a) and (b). The longitudinal leakage field forms a travelling wave that follows the driving beam, with an amplitude up to 1.0 TV/m, as seen in Fig.2 (a) and (c). The wavelength is $\lambda_{\text{SP,PIC}} = 0.52 \mu\text{m}$. This is in good agreement with the theoretical resonant surface plasmon (SP) wavelength, $\sqrt{2}\lambda_{\text{eff}} \simeq 0.47 \mu\text{m}$ [7], where λ_{eff} is calculated based on the effective wall density n_{eff} . Therefore, this field is suitable for sub-fs-level charged particle acceleration. The acceleration field within the channel is observed to be radially uniform, ensuring that the energy spectrum and beam divergence of the witness beam remain preserved throughout the acceleration process.

The transverse field, e.g. defined as $W_x = E_x - cB_y$ in x -direction, where E_x and B_y are the transverse electric and magnetic fields in x - and y -directions, respectively, can also shallowly leak into the vacuum region, providing a confining force for both positrons in the vacuum and also preventing electrons from crossing the inner surface, as shown in Fig. 2(d). The case of transverse field in y -direction is similar and will not be shown here. If an electron lacks sufficient transverse momentum, it will be confined either within the CNT wall or in the vacuum region. The transverse field is negligible in the centre region of the vacuum channel, which is highly beneficial as it enables the acceleration of both positively and negatively charged beams while preserving beam quality. Notably, the bundle CNT target also supports a similar leakage field structure, with marginally higher field amplitudes than the porous target. However, it exhibits unstable oscillations, as seen in Fig. 2(c) and (d). This variation suggests that the internal structure of the CNT wall influences the properties of the leakage field and should be optimised.

To test the acceleration process for both electrons and positrons, two simulations are conducted: one with a witness electron beam following the driving beam and the other with a witness positron beam. The witness beams have identical parameters to the driving beam, except for their reduced charge of 0.01 nC and shortened length of 0.1 μm . Both witness beams are initially placed in the first acceleration phase, positioned at 1.44 μm behind the driving beam for the electron case and 1.18 μm for the positron case, as shown in Fig. 2(a) and (c). The energy spectrum of witness and driving beams are compared in Fig.3(a). The witness beam gained energy, while the driving beam lost energy. The mean energy of the driving beam decreased by 16.7 MeV, yielding an average energy depletion

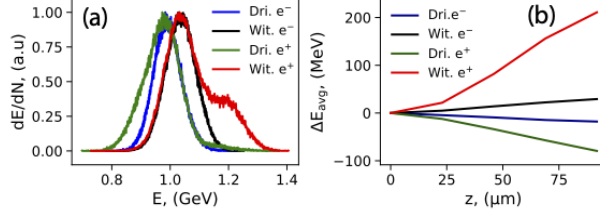


Figure 3. PIC results from two runs with either electron (blue and black) or positron (green and red) witness beams. In both simulations, the driving beams are the same. (a) Energy spectrum after 89 μm propagation in CNT channel for witness electron (black) and its driving (blue) beams, and for positron (red) and its driving (green) beams. (b) Evolution of mean energy for witness and driving beam. The colour scheme is the same as (a).

rate of $R_D = 0.19$ TeV/m. The high energy depletion is primarily driven by excitation of the bulk and surface plasmons and determined by the beam-to-target density ratio n_b/n_t [7]. Simultaneously, the mean energy of the witness electron beam is increased by 29.7 MeV, as shown in Fig.3(b), leading to a mean acceleration gradient of $G = 0.33$ TeV/m. For the positron beam, there is an additional energy gain directly from the driving beam, which leads to additional energy gain, and the mean energy is increased to 210 MeV. The mean acceleration gradient can reach up to $G = 2.36$ TeV/m. In this case, the corresponding average energy depletion rate of the driving beam is $R_D = 1.12$ TeV/m. These results align well with the leakage field amplitudes shown in Fig.2(a) and (c), demonstrating field strengths 1–3 orders of magnitude higher than the acceleration gradients typically achieved in gaseous plasma-based LWFA and PWFA[4, 5]. Moreover, the relatively low n_b/n_t suggests that such an experiment is feasible with existing facilities. For example, with a CNT target density of $n_t = 10^{20}$, cm^{-3} , a beam density as low as $n_b = 10^{18}$, cm^{-3} would be sufficient conditions achievable at facilities like FACET-II at SLAC [44] or in the upgraded CLARA facility at Daresbury Laboratory [45].

However, it is important to also note that the acceleration gradient G is still 2 orders of magnitude lower than the coherent field limit E_{wb} predicted for the CNT wall density n_t used in these simulations. This indicates that only a small fraction of the plasmon energy is leaking into the vacuum channel for acceleration, resulting in relatively low energy efficiency. The energy transfer efficiency, defined as the ratio of energy gained by the witness beam to the total energy lost from the driving beam after 89 μm propagation, is given for positron

acceleration by

$$\eta_{SPs} = \frac{\int_{V_b} \mathcal{E}_b n_b d\mathbf{r}}{\int_{V_w} \mathcal{E}_w n_w d\mathbf{r}} \simeq 7.1\%, \quad (3)$$

where the symbols b and w denote driving and witness beam respectively. $\mathcal{E}_{b,w}$ denotes the energy spectrum, $n_{b,w}$ the beam density distribution and $V_{b,w}$ the beam volume, respectively. For the electron case, $\eta_{SPs} = 6\%$. The relatively low strength of the acceleration field and then the transfer efficiency are attributed to the fact that the conduction electrons, as the primary energy carrier, cannot transit across the inner surface.

IV. BUBBLE WAKEFIELD EXCITATION AND ACCELERATION

To drive the conduction electron crossing the inner surfaces, a higher-density driving beam with a total charge of 10 nC and a density of $1.0 \times 10^{22} \text{ cm}^{-3}$ or $n_b/n_t = 0.5$ is considered. The initial beam energy is 10 GeV.

The nonlinear plasma wakefield, also known as bubble wakefield, is excited inside the vacuum channel after the driving beam travels $47 \mu\text{m}$ through the CNT target as shown in Fig. 4. This process also triggers self-injection. The resulting plasma bubble is similar to that in gaseous plasma [1], but with the exceptionally high amplitude of the acceleration field, reaching up to 83 TV/m. This value is nearly an order of magnitude higher than the coherent field limit E_{wb} , estimated from n_{eff} . The longitudinal acceleration field is also radially uniform, which enhances beam quality. This amplified field strength results from the confinement of transited wall electrons, preventing them from escaping the vacuum channel, as well as from mitigating bubble breaking. Unlike typical uniform plasma bubbles, the acceleration volume extends $2 \mu\text{m}$ in the longitudinal and $3 \mu\text{m}$ in the transverse dimensions, which is significantly larger than that of a typical plasma wave of same density. This larger volume supports the acceleration of high-charge witness beams with sizes that fit the aforementioned dimensions.

In the transverse direction, the wakefield does not significantly leak into the vacuum channel but instead creates a strong focusing field within the CNT wall, reaching an amplitude of 100 TV/m. This phenomenon occurs because the conduction electrons are compressed away from the inner surface, while the transverse wakefield W_x is effectively shielded by the ionic lattice. This feature makes the system promising for both electron and positron acceleration within the vacuum region, where the transverse field vanishes [46–48]. It also

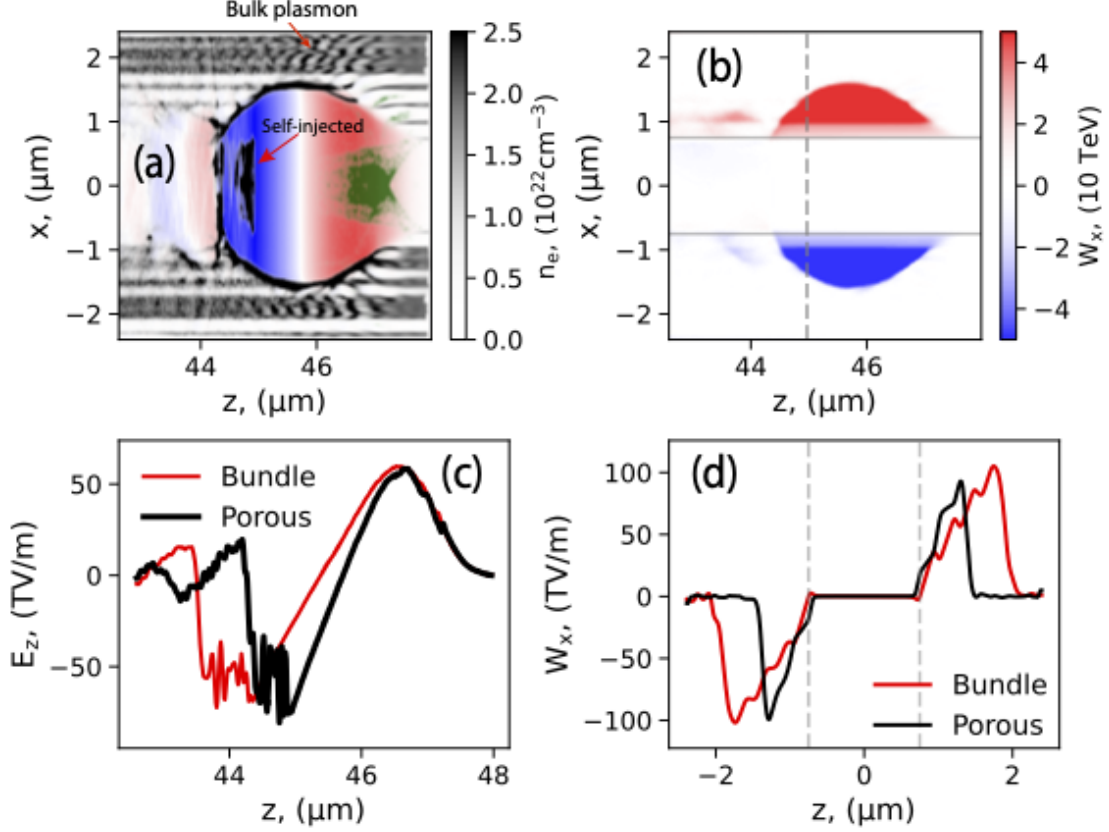


Figure 4. PIC results: Bubble wakefield excitation in nanostructured CNT targets. (a) Slice of conduction electron density distribution (grey colourmap), E_z (red-blue colourmap), and driving beams (green colourmap). (b) Slice of W_x . (c) On-axis ($x = 0$) plot of E_z for porous (black) and bundle (red) targets. (d) Line plot of W_x for porous (black) and bundle (red) targets at $z = 48 \mu\text{m}$, indicated by the vertical dashed grey line in (b).

helps the driving beam channelling stably. For positron acceleration, the optimal phase is located in the second plasma bubble around $z = 44 \mu\text{m}$, as shown in Fig.4(a), where the field amplitude reaches up to 15 TV/m. This value is 2-4 orders of magnitude higher than typical field strengths in gaseous plasmas [4, 5]. However, in the current simulations, the field volume is relatively small and unstable, highlighting the need for optimisation, such as using lower-density targets or a positively charged driving beam.

Bulk plasmon oscillation is also observed within the CNT wall, with a simulated wavelength of $\lambda_{p,\text{PIC}} = 0.22 \mu\text{m}$, closely matching the theoretical value of $\lambda_p = 0.235 \mu\text{m}$ [7]. The bundle target exhibits a similar wakefield structure, as shown in Fig. 4(b) and (c), with some differences in the spatial dimensions of the plasma bubble. This consistency vali-

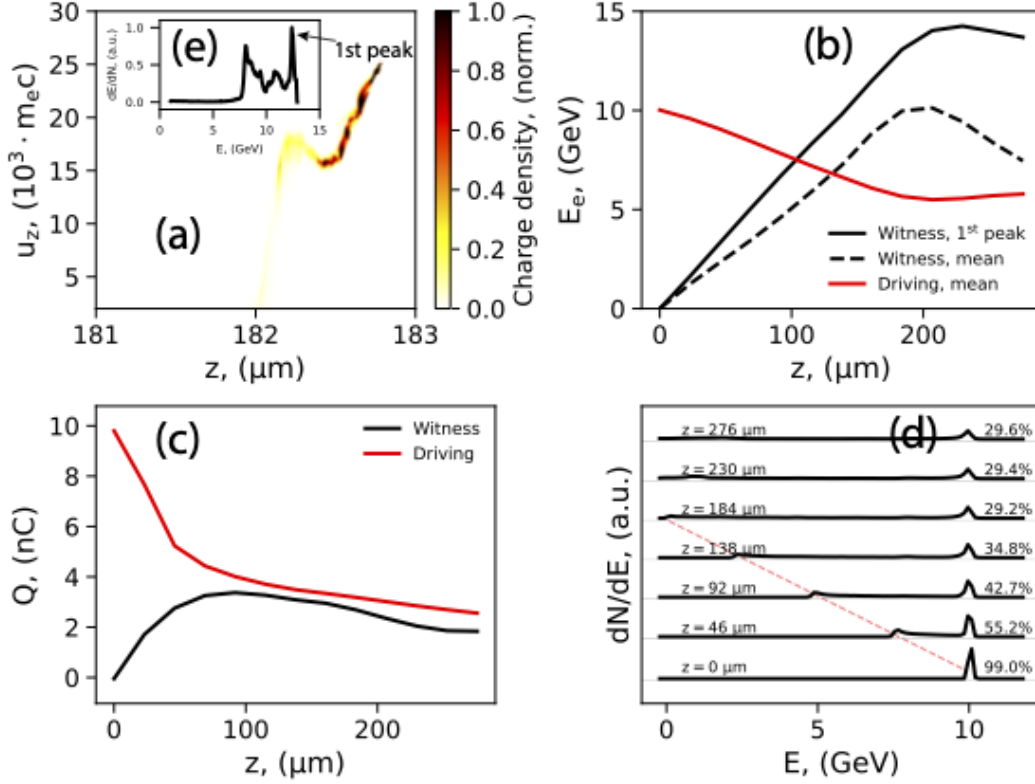


Figure 5. PIC simulation results: (a) Longitudinal phase space of accelerated electrons of the kinetic energy above 200 MeV after leaving the 180 μm -long porous target. (b) Energy evolution: red solid: mean energy gain of the driving beam; Black solid: peak energy in energy spectrum indicated in (e); black dashed: mean energy of self-trapped electrons of the kinetic energy above 200 MeV, respectively. (c) Evolution of charge of the accelerated electrons (black) and driving beam (red). (d) Energy spectrum of the driving beam at different propagation distances. (e) Energy spectrum of accelerated electrons. The parameters used are the same as those in Fig. 2 except for the charge of the driving beam.

dates the effective density model [38, 49] while also highlighting the influence of the specific nanostructure on the wakefield dynamics.

The ultra-high accelerating and focusing field enables the transmitted electrons to be accelerated efficiently and then trapped into the plasma wave by channeling through the vacuum channel for a long distance. The energy spectrum of the accelerated electrons, shown in Fig. 5(a) and (e) after the driving beam propagates 182 μm , is quasi-monoenergetic, featuring two peaks. The high-energy peak is at 13.0 GeV with a 1% energy spread, and

the lower peak is at 8.5 GeV with a 35% spread. Fig. 5(b) and (c) illustrate the energy and charge evolutions of the driving and witness beams, respectively. The energy of the first peak reaches 14.6 GeV, corresponding to a peak acceleration gradient of $G = 73.0$ TeV/m. After propagating 200 μm , the mean energy of the self-trapped electrons attains 10 GeV, indicating a mean acceleration gradient of $G = 50.0$ TeV/m. Self-trapping saturates around $z = 100$ μm with a total charge of 3.6 nC of electrons due to significant depletion of the driving beam.

The driving beam rapidly loses energy, with its mean energy dropping to 5 GeV, and the charge of electrons above 1 GeV reduces to 3 nC. The mean energy transfer efficiency to the witness beam is then estimated as $\eta_{bw} = 66.7\%$ after a 200 μm of propagation. In this case, the ultra-high energy depletion rate of the driving beam is observed to be $R_D = 25$ TeV/m, which is 33.3 times greater than that required for leakage field excitation. Additionally, the initial high beam energy contributes to the elevated R_D value, as it extends the lifetime of the strong bubble wakefield excitation. The mean charge depletion rate of the driving beam is also significant, reaching $R_Q = 0.35$ nC/ μm . This highly efficient depletion is shown in Fig. 5(d), where a significant portion of the driving beam is lost, as indicated by the red dashed line. After $z = 200$ μm , only 29% of the high-energy electrons remain insufficient to sustain the strong wakefield. At this point, the total charge of the witness beam balances with the driving beam, as shown in Fig. 5(c). As the energy or charge of the driving beam depletes, the energy transfer ceases, and the witness beam begins to lose energy and charge to the target. This indicates the maximum propagation distance of a driving beam inside a CNT channel, referred to the depletion limit L_p , which is crucial for performance. To extend L_p , higher beam charge Q_b or target density n_t should be considered.

V. BLOWOUT REGIME

When the driving beam charge Q_b , and consequently the beam density, becomes sufficiently high, the wall electrons experience the full blowout, escaping the finite CNT wall structure [49]. This occurs when the outward Coulomb force exerted by the driving beam exceeds the restoring force from the wall ions. The full blowout conditions can be readily

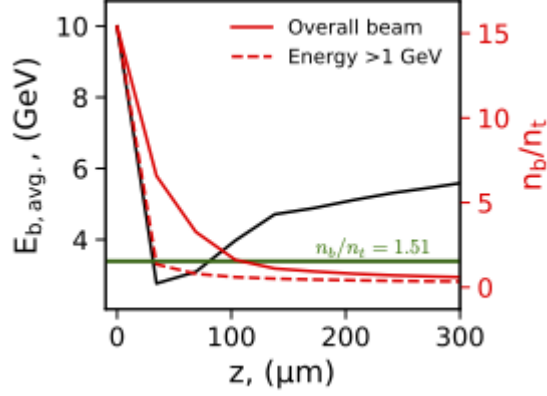


Figure 6. Evolution of mean energy of overall beam (black solid) and evolution of n_b/n_t of overall electron (red solid) and electrons of energy above 1 GeV (red dashed). The horizontal green line indicates the blowout condition.

estimated by balancing the beam force as $F_{\text{beam}} \sim n_b V_b > F_{\text{ion}} \sim n_{\text{eff}} V_{\text{wall}}$ where

$$\frac{n_b}{n_{\text{eff}}} = \frac{V_{\text{wall}}}{V_b} = \frac{\Delta w(2r_t + \Delta w)}{\sigma_{r0}^2}, \quad (4)$$

where $\Delta w = (N - 1)g + Nd$ is the wall width. V_b and V_{wall} are transverse beam and wall volume respectively. Under the parameters used here, the blowout occurs when $n_b > 3.02n_{\text{eff}} = 3.0 \times 10^{22} \text{ cm}^{-2}$ or $n_b/n_t > 1.51$. This implies that the blowout does not occur under the previous simulation conditions. Be noticed that since Eq. (4) is derived based on the effective wall density, n_{eff} , it applies to both porous and bundled CNT targets. Therefore, in the following simulations, only porous targets are considered.

To explore this, a new PIC simulation uses a 200 nC driving beam, giving $n_b/n_t = 15.4$. The energy and charge evolutions are shown in Fig. 6. The blowout happens when the beam density significantly surpasses the threshold $n_b/n_t = 1.51$ before $z = 35 \mu\text{m}$, causing all conduction electrons to be stripped away from the CNT wall, preventing the generation of an acceleration field. At the same time, the beam charge of high-energy electrons is rapidly depleted to below the threshold $n_b/n_t < 1.51$, where the blowout stops and the charge depletion slows down, leaving only 20 nC. The mean charge depletion rate during the blowout section can be estimated as $R_Q = 5.14 \text{ nC}/\mu\text{m}$. Along with charge loss, the beam energy (black solid line) is also rapidly depleted, particularly for the electrons with energies above 1 GeV. These electrons lose energy, becoming low-energy electrons, and are subsequently expelled from the vacuum channel by streaming backwards as the confining

potential of the inner surfaces prevents their transverse escape. The observed delay between the charge loss of high-energy electrons (red dashed line) and the overall beam electron loss (red solid line) in the moving window indicates a cascading process. In this process, energy and charge are predominantly lost from the head of the beam, while the tail remains largely unaffected, similar to the energy depletion in the plasma dump [50]. The bubble wakefield is excited between $35 \mu\text{m} < z < 130 \mu\text{m}$ once the beam density falls below the blowout threshold. During this interval, energy and high-energy charge depletion are significantly reduced. However, as low-energy electrons continue to be lost, the mean energy of the remaining beam increases. After $130 \mu\text{m}$, the n_b/n_t ratio of high-energy electrons falls below 0.01, resulting in the generation of surface plasmons (SPs) with lower energy and charge depletion rate. This behaviour is notable as it demonstrates that the solid-density CNT target scheme is dynamically stable and can be effectively scaled by adjusting the n_b/n_t ratio, thus offering a promising level of practical robustness.

VI. DISCUSSION AND SUMMARY

The fundamental assumption in this work is that the wall density of the CNT target is sufficiently high for the conduction electron gas to be quantum degenerated and correlated. In this regime, the electrons can be approximated as classical free electrons, allowing for the use of classical PIC simulations to study this phenomenon. Alternatively, with the low-density CNT wall, the temperature should be low in order to sustain the quantum degeneracy as shown in Fig. 7(a) where, for example, the system can support significantly lower beam densities without breaking degeneracy at $T = 100$ K.

Due to the solid-state surface, the excitation of SPs dominates the plasma dynamics. This occurs as a result of the balance between the ionic forces of the CNT wall and the Coulomb force from the electrons, which is influenced by the beam-to-plasma density ratio n_b/n_t , as illustrated in Fig. 7(b). The coherent plasma dynamics in the CNT target is significantly different from that in the gaseous plasma and similar to what is observed in previous studies on hollow plasma channels [46, 48]. At low beam-to-plasma density ratios (e.g., $n_b/n_t < 0.01$), the transverse momentum of the wall electrons remains low, preventing them from emitting into the core vacuum region. As a result, SP modes are excited along the wall surface. These SP modes behave as pure EM waves that can leak into the vacuum channel,

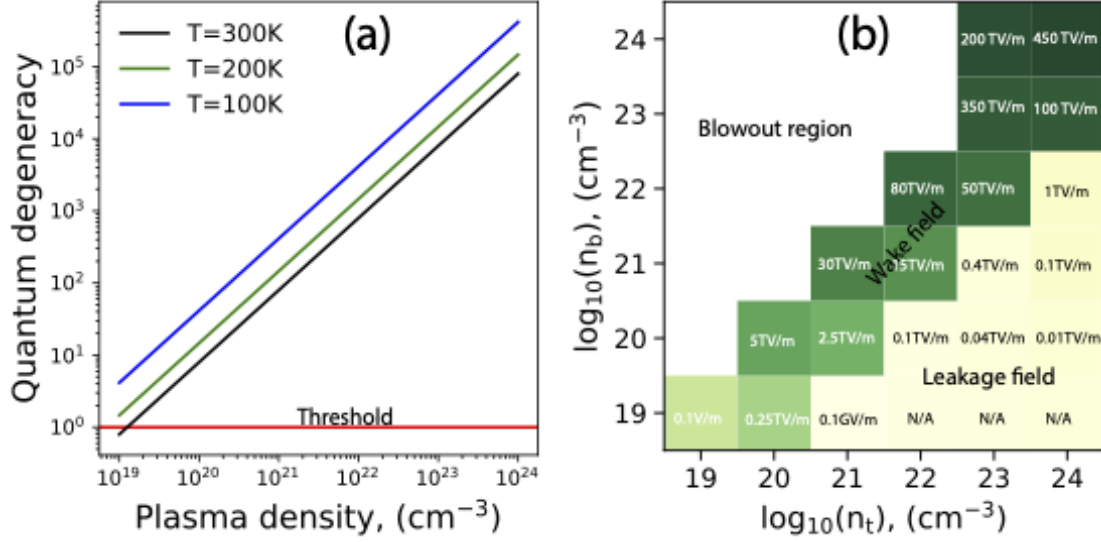


Figure 7. (a) Theory: quantum degeneracy as a function of CNT wall density for different temperatures. (b) PIC results: Diagram of peak acceleration field of porous CNT target with 6 different initial beam n_b and plasma density n_t , $1 \times 10^{19,20,21,22,23,24}$ cm^{-3} . The yellow colour area indicates the region for the leakage field, the green area for the bubble wakefield, and the white area for the blowout. PIC simulations are performed by varying n_t and total beam charge Q_b independently and keeping the other parameters the same.

providing a sub-TV/m acceleration field while being automatically phase matched for both electron and positron acceleration. With the moderately high beam density comparable with CNT wall density n_t , the transited wall electrons lead to the excitation of the bubble wakefield in the vacuum channel, forming bubbles similar to those observed in gaseous plasmas. The field is electrostatic, and the amplitude scales up to 450 TV/m with the used parameters. However, the excitation of such ultra-high acceleration fields necessitates an ultra-high energy and charge pumping rate from the driving beam. This, in turn, can cause energy-depleted driving electrons to stream backwards, limiting the maximum pumping length and leading to the deterioration of the witness beam quality, including significant energy and charge loss. The issue of backward streaming can potentially be mitigated by employing a laser pulse. Additionally, the pumping problem can be improved by optimising the parameters of the driving beam and target configuration. Finally, full blowout occurs when the beam density exceeds the threshold, as shown in Eq. (4), where no acceleration field exists. However, along with the driving beam rapidly depletes and the beam density

n_b decreases, it may still be possible to excite both the wake and leakage fields, allowing for continued acceleration.

As shown in Fig. 7(b), 36 simulations were conducted with 6 distinct values of each n_t and n_b , where the white coloured area represents the blowout regime, the green area is the bubble wakefield regime and the yellow area corresponds to the SPs regime. The acceleration field amplitude can exceed 400 TV/m if n_b and n_t can be prepared at the 10^{24} cm^{-3} level. This demonstrates substantial potential for the development of CNT-based accelerators capable of accelerating electrons to PeV energies over meter distances. However, achieving such high-density beams poses a significant challenge with current state-of-the-art facilities. For example, a 1 nC electron bunch with a duration of 100s attoseconds needs to be a transverse size of hundreds of nm to achieve a beam density close to $n_b \sim 10^{24} \text{ cm}^{-3}$. This level of compression may be possible with future bunch compressor chicanes, such as the one proposed for FACET-II at SLAC [44], which anticipates a 125 GeV electron beam with a density up to 10^{34} cm^{-3} . In current stage, FACET-II will be capable of delivering 3 nC electron and positron beams at 10 GeV with a transverse size of down to $0.25 - 2 \mu\text{m}$ and a duration of $0.5 \mu\text{m}$. This could result in a beam density in the range of $10^{20-22} \text{ cm}^{-3}$, sufficient to drive the bubble wakefields of acceleration gradient on the order of tens of TeV/m, or even trigger blowout. With other novel electron sources, such as, electron beam from X-ray free electron lasers facilities [51], or LWFA and PWFA, a relatively weak bubble wakefield can be excited if the beam can be further compressed. Facilities like CLARA [45], which can provide 250 MeV, sub-nC-level electron beams, could also play a role. If such beams can be compressed to μm -level by, e.g. plasma lenses [52, 53] where transverse focusing by 1-2 orders of magnitude is possible, the peak density could reach $10^{18-19} \text{ cm}^{-3}$. This would be sufficient to drive leakage fields with TV/m acceleration, enabling proof-of-principle experiments. The target length could be extended to tens of micrometers, potentially achieving energy gains of 10s MeV/ μm .

In summary, the CNT-based solid-state plasma accelerator offers transformative potential for advancing the development of ultra-compact particle accelerators, opening new avenues for various advanced applications. For example, the ultra-high acceleration gradient to accelerate both negatively and positively charged particles to several GeV in fs time scale, which is much shorter than the finite mean lifetime of muons, $2.2 \mu\text{s}$ at rest [54]. The ultra-high energy and charge pumping rate make it highly suitable for applications such as high-

energy beam dump or recycle facilities [50, 55]. Combined with the excellent mechanical, thermal, and electrical properties of nanostructured CNT targets, this technology offers a highly efficient and safe option for managing high-energy beams. The ultra-strong EM fields, reaching amplitudes of several hundred TV/m over several μm spatial dimensions, highlight its potential for even more advanced applications, such as strong-field physics [56], astrophysics [57], and particle physics [58], where extreme field strengths are crucial for exploring new physical regimes.

Nevertheless, critical gaps remain in our understanding of key physical processes that are essential for fully understanding the excitation of SPs and the generation of ultra-high bubble wakefield acceleration fields—nearly an order of magnitude higher than the theoretical limit for coherent wakefields. While some negative effects, such as limited depletion length and low energy, have been investigated and explained for homogeneous gaseous plasmas [50], further investigation is required to verify the behaviour of the driving beam energy loss in the proposed targets. Alongside advancements in nanofabrication technology, the CNT-based plasma accelerator presented in this work demands driving beams of extreme quality, posing a significant challenge for practical implementation.

Emerging beam compression techniques [52, 53, 59] hold promise in delivering high-density particle beams with transverse dimensions on the order of hundreds of nanometers. These advances will significantly contribute to experimental progress, enabling proof-of-concept experiments at currently accessible facilities, such as CLARA and FACET-II. A practical compromise might involve using doped semiconductor materials, which can provide free plasma electrons with densities around 10^{18} cm^{-3} . This could easily be matched with currently available beams that have spatial sizes of $10 \mu\text{m}$ and similar densities, achieving acceleration gradients in the tens of GeV/m range.

In addition to lasers and negatively charged particle beams, high-energy positively charged beams—such as positrons or protons [12, 60]—could also potentially drive significant bubble wakefield modes within a CNT channel. International laboratories like SLAC and CERN could provide access to such beams. Given the similar plasma dynamics, it will be important to further investigate whether these beams display distinct differences in beam modulation and wakefield behaviour and if such differences could offer advantages for acceleration and other applications.

ACKNOWLEDGMENTS

Javier Resta-López acknowledges support by the Generalitat Valenciana under grant agreement CIDEAGENT/2019/058. This work made use of the facilities of the N8 Centre of Excellence in Computationally Intensive Research (N8 CIR) provided and funded by the N8 research partnership and EPSRC (Grant No. EP/T022167/1). The Centre is coordinated by the Universities of Durham, Manchester and York.

-
- [1] E. Esarey, C. B. Schroeder, and W. P. Leemans, Physics of laser-driven plasma-based electron accelerators, [Rev. Mod. Phys.](#) **81**, 1229 (2009).
 - [2] T. Tajima and J. M. Dawson, Laser electron accelerator, [Phys. Rev. Lett.](#) **43**, 267 (1979).
 - [3] P. Chen, J. M. Dawson, R. W. Huff, and T. Katsouleas, Acceleration of electrons by the interaction of a bunched electron beam with a plasma, [Phys. Rev. Lett.](#) **54**, 693 (1985).
 - [4] E. Adli, A. Ahuja, O. Apsimon, R. Apsimon, A. M. Bachmann, D. Barrientos, F. Batsch, J. Bauche, V. K. Berglyd Olsen, M. Bernardini, T. Bohl, C. Bracco, F. Braunmüller, G. Burt, B. Buttenschön, A. Caldwell, M. Cascella, J. Chappell, E. Chevallay, M. Chung, D. Cooke, H. Damerau, L. Deacon, L. H. Deubner, A. Dexter, S. Doebert, J. Farmer, V. N. Fedosseev, R. Fiorito, R. A. Fonseca, F. Friebe, L. Garolfi, S. Gessner, I. Gorgisyan, A. A. Gorn, E. Granados, O. Grulke, E. Gschwendtner, J. Hansen, A. Helm, J. R. Henderson, M. Hüther, M. Ibison, L. Jensen, S. Jolly, F. Keeble, S. Y. Kim, F. Kraus, Y. Li, S. Liu, N. Lopes, K. V. Lotov, L. Maricalva Brun, M. Martyanov, S. Mazzoni, D. Medina Godoy, V. A. Minakov, J. Mitchell, J. C. Molendijk, J. T. Moody, M. Moreira, P. Muggli, E. Öz, C. Pasquino, A. Pardons, F. Peña Asmus, K. Pepitone, A. Perera, A. Petrenko, S. Pitman, A. Pukhov, S. Rey, K. Rieger, H. Ruhl, J. S. Schmidt, I. A. Shalimova, P. Sherwood, L. O. Silva, L. Soby, A. P. Sosedkin, R. Speroni, R. I. Spitsyn, P. V. Tuv, M. Turner, F. Velotti, L. Verra, V. A. Verzilov, J. Vieira, C. P. Welsch, B. Williamson, M. Wing, B. Woolley, and G. Xia, Acceleration of electrons in the plasma wakefield of a proton bunch, [Nature](#) **561**, 363 (2018).
 - [5] A. J. Gonsalves, K. Nakamura, J. Daniels, C. Benedetti, C. Pieronek, T. C. H. de Raadt, S. Steinke, J. H. Bin, S. S. Bulanov, J. van Tilborg, C. G. R. Geddes, C. B. Schroeder, C. Tóth, E. Esarey, K. Swanson, L. Fan-Chiang, G. Bagdasarov, N. Bobrova, V. Gasilov, G. Korn,

- P. Sasorov, and W. P. Leemans, Petawatt laser guiding and electron beam acceleration to 8 gev in a laser-heated capillary discharge waveguide, *Phys. Rev. Lett.* **122**, 084801 (2019).
- [6] D. Pines, A collective description of electron interactions: Iv. electron interaction in metals, *Phys. Rev.* **92**, 626 (1953).
- [7] R. H. Ritchie, Plasma losses by fast electrons in thin films, *Phys. Rev.* **106**, 874 (1957).
- [8] T. Tajima, Laser acceleration in novel media, *The European Physical Journal Special Topics* **223**, 1037 (2014).
- [9] M. F. Gilljohann, Y. Mankovska, P. San Miguel Claveria, A. Sytov, L. Bandiera, R. Ariniello, X. Davoine, H. Ekerfelt, F. Fiuza, L. Gremillet, A. Knetsch, B. Martinez, A. Matheron, H. Piekarz, D. Storey, P. Taborek, T. Tajima, V. Shiltsev, and S. Corde, Channeling acceleration in crystals and nanostructures and studies of solid plasmas: new opportunities, *Journal of Instrumentation* **18** (11), P11008.
- [10] S. Chattopadhyay, G. Mourou, V. D. Shiltsev, and T. Tajima, *Beam Acceleration in Crystals and Nanostructures* (WORLD SCIENTIFIC, 2020) p. 268.
- [11] Y.-M. Shin, Carbon nanotube accelerator —path toward tev/m acceleration: Theory, experiment, and challenges, *International Journal of Modern Physics A* **34**, 1943005 (2019).
- [12] X. Zhang, T. Tajima, D. Farinella, Y. Shin, G. Mourou, J. Wheeler, P. Taborek, P. Chen, F. Dollar, and B. Shen, Particle-in-cell simulation of x-ray wakefield acceleration and betatron radiation in nanotubes, *Phys. Rev. Accel. Beams* **19**, 101004 (2016).
- [13] H. Gleiter, Nanostructured materials: basic concepts and microstructure, *Acta Materialia* **48**, 1 (2000).
- [14] S. Xiao, T. Wang, T. Liu, C. Zhou, X. Jiang, and J. Zhang, Active metamaterials and metadevices: a review, *Journal of Physics D: Applied Physics* **53**, 503002 (2020).
- [15] C. Bonțoiu, Ö. Apsimon, E. Kukstas, V. Rodin, M. Yadav, C. Welsch, J. Resta-López, A. Bonatto, and G. Xia, Tev/m catapult acceleration of electrons in graphene layers, *Scientific Reports* **13**, 1330 (2023).
- [16] N. M. Naumova, J. A. Nees, I. V. Sokolov, B. Hou, and G. A. Mourou, Relativistic generation of isolated attosecond pulses in a λ^3 focal volume, *Phys. Rev. Lett.* **92**, 063902 (2004).
- [17] G. Mourou, S. Mironov, E. Khazanov, and A. Sergeev, Single cycle thin film compressor opening the door to zeptosecond-exawatt physics, *The European Physical Journal Special Topics* **223**, 1181 (2014).

- [18] A. Eatemadi, H. Daraee, H. Karimkhanloo, M. Kouhi, N. Zarghami, A. Akbarzadeh, M. Abasi, Y. Hanifehpour, and S. W. Joo, Carbon nanotubes: properties, synthesis, purification, and medical applications, *Nanoscale Research Letters* **9**, 393 (2014).
- [19] S. Rathinavel, K. Priyadharshini, and D. Panda, A review on carbon nanotube: An overview of synthesis, properties, functionalization, characterization, and the application, *Materials Science and Engineering: B* **268**, 115095 (2021).
- [20] E. A. Stern and R. A. Ferrell, Surface plasma oscillations of a degenerate electron gas, *Phys. Rev.* **120**, 130 (1960).
- [21] T. Tajima and S. Ushioda, Surface polaritons in lo-phonon-plasmon coupled systems in semiconductors, *Physical Review B* **18**, 1892 (1978).
- [22] M. S. Ukhtary and R. Saito, Surface plasmons in graphene and carbon nanotubes, *Carbon* **167**, 455 (2020).
- [23] P. Martín-Luna, A. Bonatto, C. Bontoiu, G. Xia, and J. Resta-López, Plasmonic excitations in double-walled carbon nanotubes, *Results in Physics* **60**, 107698 (2024).
- [24] D. N. Futaba, K. Hata, T. Namai, T. Yamada, K. Mizuno, Y. Hayamizu, M. Yumura, and S. Iijima, 84% catalyst activity of water-assisted growth of single walled carbon nanotube forest characterization by a statistical and macroscopic approach, *The Journal of Physical Chemistry B* **110**, 8035 (2006).
- [25] S. Iijima, Helical microtubules of graphitic carbon, *Nature* **354**, 56 (1991).
- [26] W. Yang, X.-G. Zheng, S.-G. Wang, and H.-J. Jin, Nanoporous aluminum by galvanic replacement: Dealloying and inward-growth plating, *Journal of The Electrochemical Society* **165**, C492 (2018).
- [27] P. Chen and R. J. Noble, A solid state accelerator, *AIP Conference Proceedings* **156**, 222 (1987).
- [28] A. Benedetti, M. Tamburini, and C. H. Keitel, Giant collimated gamma-ray flashes, *Nature Photonics* **12**, 319 (2018).
- [29] X. fu Zong, C. Shen, S. Liu, Z. Wu, Y. Chen, R. Zhang, J. G. Zhu, Y. Chen, B. D. Evans, R. González, and C. H. Sellers, Radiation induced electrical degradation in crystalline al₂o₃: a bulk effect, *Journal of Nuclear Materials* **219**, 176 (1995).
- [30] S. J. Gamble, M. H. Burkhardt, A. Kashuba, R. Allenspach, S. S. P. Parkin, H. C. Siegmann, and J. Stöhr, Electric field induced magnetic anisotropy in a ferromagnet, *Phys. Rev. Lett.*

- [102](#), [217201](#) (2009).
- [31] G. E. Thompson, Porous anodic alumina: fabrication, characterization and applications, *Thin Solid Films* **297**, 192 (1997).
- [32] T. Kyotani, Synthesis of various types of nano carbons using the template technique, *Bulletin of the Chemical Society of Japan* **79**, 1322 (2006).
- [33] P. Hou, C. Liu, C. Shi, and H. Cheng, Carbon nanotubes prepared by anodic aluminum oxide template method, *Chinese Science Bulletin* **57**, 187 (2012).
- [34] E. Joselevich, H. Dai, J. Liu, K. Hata, and A. H. Windle, Carbon nanotube synthesis and organization, in *Carbon Nanotubes: Advanced Topics in the Synthesis, Structure, Properties and Applications*, edited by A. Jorio, G. Dresselhaus, and M. S. Dresselhaus (Springer Berlin Heidelberg, Berlin, Heidelberg, 2008) pp. 101–165.
- [35] C. H. See and A. T. Harris, A review of carbon nanotube synthesis via fluidized-bed chemical vapor deposition, *Industrial & Engineering Chemistry Research* **46**, 997 (2007).
- [36] E. Schifano, G. Cavoto, F. Pandolfi, G. Pettinari, A. Apponi, A. Ruocco, D. Uccelletti, and I. Rago, Plasma-etched vertically aligned cnts with enhanced antibacterial power, *Nanomaterials* **13**, [10.3390/nano13061081](#) (2023).
- [37] R. P. Yadav, I. Rago, F. Pandolfi, C. Mariani, A. Ruocco, S. Tayyab, A. Apponi, and G. Cavoto, Evaluation of vertical alignment in carbon nanotubes: A quantitative approach, *Nuclear Instruments and Methods in Physics Research Section A: Accelerators, Spectrometers, Detectors and Associated Equipment* **1060**, 169081 (2024).
- [38] A. Bonatto, G. Xia, O. Apsimon, C. Bontoiu, E. Kukstas, V. Rodin, M. Yadav, C. P. Welsch, and J. Resta-López, Exploring ultra-high-intensity wakefields in carbon nanotube arrays: An effective plasma-density approach, *Physics of Plasmas* **30**, 033105 (2023).
- [39] S. Hakimi, T. Nguyen, D. Farinella, C. K. Lau, H.-Y. Wang, P. Taborek, F. Dollar, and T. Tajima, Wakefield in solid state plasma with the ionic lattice force, *Physics of Plasmas* **25**, [023112](#) (2018).
- [40] L. Fedeli, A. Huebl, F. Boillod-Cerneux, T. Clark, K. Gott, C. Hillairet, S. Jaure, A. Leblanc, R. Lehe, A. Myers, C. Piechurski, M. Sato, N. Zaim, W. Zhang, J.-L. Vay, and H. Vincenti, Pushing the frontier in the design of laser-based electron accelerators with groundbreaking mesh-refined particle-in-cell simulations on exascale-class supercomputers, in *SC22: International Conference for High Performance Computing, Networking, Storage and Analysis* (2022)

pp. 1–12.

- [41] M. V. Ammosov, N. B. Delone, and V. P. Krainov, *Tunnel ionization of complex atoms and atomic ions in electromagnetic field* (SPIE Society of Photo-Optical Instrumentation Engineers, United States, 1986).
- [42] S. Suzuki, C. Bower, Y. Watanabe, and O. Zhou, Work functions and valence band states of pristine and Cs-intercalated single-walled carbon nanotube bundles, *Applied Physics Letters* **76**, 4007 (2000).
- [43] H. Ago, T. Kugler, F. Cacialli, W. R. Salaneck, M. S. P. Shaffer, A. H. Windle, and R. H. Friend, Work functions and surface functional groups of multiwall carbon nanotubes, *The Journal of Physical Chemistry B* **103**, 8116 (1999).
- [44] V. Yakimenko, L. Alsberg, E. Bong, G. Bouchard, C. Clarke, C. Emma, S. Green, C. Hast, M. J. Hogan, J. Seabury, N. Lipkowitz, B. O’Shea, D. Storey, G. White, and G. Yocky, Facet-ii facility for advanced accelerator experimental tests, *Phys. Rev. Accel. Beams* **22**, 101301 (2019).
- [45] E. W. Snedden, D. Angal-Kalinin, A. R. Bainbridge, A. D. Brynes, S. R. Buckley, D. J. Dunning, J. R. Henderson, J. K. Jones, K. J. Middleman, T. J. Overton, T. H. Pacey, A. E. Pollard, Y. M. Saveliev, B. J. A. Shepherd, P. H. Williams, M. I. Colling, B. D. Fell, and G. Marshall, Specification and design for full energy beam exploitation of the compact linear accelerator for research and applications, *Phys. Rev. Accel. Beams* **27**, 041602 (2024).
- [46] C. B. Schroeder, E. Esarey, C. Benedetti, and W. P. Leemans, Control of focusing forces and emittances in plasma-based accelerators using near-hollow plasma channels, *Physics of Plasmas* **20**, 080701 (2013).
- [47] S. Gessner, E. Adli, J. M. Allen, W. An, C. I. Clarke, C. E. Clayton, S. Corde, J. P. Delahaye, J. Frederico, S. Z. Green, C. Hast, M. J. Hogan, C. Joshi, C. A. Lindstrøm, N. Lipkowitz, M. Litos, W. Lu, K. A. Marsh, W. B. Mori, B. O’Shea, N. Vafaei-Najafabadi, D. Walz, V. Yakimenko, and G. Yocky, Demonstration of a positron beam-driven hollow channel plasma wakefield accelerator, *Nature Communications* **7**, 11785 (2016).
- [48] L. Yi, B. Shen, L. Ji, K. Lotov, A. Sosedkin, XiaomeiZhang, W. Wang, J. Xu, Y. Shi, L. Zhang, and Z. Xu, Positron acceleration in a hollow plasma channel up to tev regime, *Scientific Reports* **4**, 4171 (2014).
- [49] A. A. Sahai, Excitation of a nonlinear plasma ion wake by intense energy sources with appli-

- cations to the crunch-in regime, [Phys. Rev. Accel. Beams](#) **20**, 081004 (2017).
- [50] A. Bonatto, R. P. Nunes, B. S. Nunes, S. Kumar, L. Liang, and G. Xia, An active plasma beam dump for eupraxia beams, [Instruments](#) **5**, 10.3390/instruments5030024 (2021).
- [51] N. Huang, H. Deng, B. Liu, D. Wang, and Z. Zhao, Features and futures of x-ray free-electron lasers, [The Innovation](#) **2**, 100097 (2021).
- [52] R. Pompili, M. P. Anania, M. Bellaveglia, A. Biagioni, S. Bini, F. Bisesto, E. Brentegani, F. Cardelli, G. Castorina, E. Chiadroni, A. Cianchi, O. Coiro, G. Costa, M. Croia, D. Di Giovenale, M. Ferrario, F. Filippi, A. Giribono, V. Lollo, A. Marocchino, M. Marongiu, V. Martinelli, A. Mostacci, D. Pellegrini, L. Piersanti, G. Di Pirro, S. Romeo, A. R. Rossi, J. Scifo, V. Shpakov, A. Stella, C. Vaccarezza, F. Villa, and A. Zigler, Focusing of high-brightness electron beams with active-plasma lenses, [Phys. Rev. Lett.](#) **121**, 174801 (2018).
- [53] G. Hairapetian, P. Davis, C. E. Clayton, C. Joshi, S. C. Hartman, C. Pellegrini, and T. Katsouleas, Experimental demonstration of dynamic focusing of a relativistic electron bunch by an overdense plasma lens, [Phys. Rev. Lett.](#) **72**, 2403 (1994).
- [54] K. R. Long, D. Lucchesi, M. A. Palmer, N. Pastrone, D. Schulte, and V. Shiltsev, Muon colliders to expand frontiers of particle physics, [Nature Physics](#) **17**, 289 (2021).
- [55] E. Lopez Sola, M. Calviani, P. Avigni, M. Battistin, J. Busom Descarrega, J. Canhoto Espadanal, M. A. Fraser, S. Gilardoni, B. Goddard, D. Grenier, R. Jacobsson, K. Kershaw, M. Lamont, A. Perillo-Marcone, M. Pandey, B. Riffaud, S. Sgobba, V. Vlachoudis, and L. Zuccalli, Design of a high power production target for the beam dump facility at cern, [Phys. Rev. Accel. Beams](#) **22**, 113001 (2019).
- [56] K. Hattori, K. Itakura, and S. Ozaki, Strong-field physics in qed and qcd: From fundamentals to applications, [Progress in Particle and Nuclear Physics](#) **133**, 104068 (2023).
- [57] B. A. Remington, High energy density laboratory astrophysics, [Plasma Physics and Controlled Fusion](#) **47**, A191 (2005).
- [58] J. T. Mendonça, H. Terças, and J. D. Rodrigues, Axion excitation by intense laser fields in a plasma, [Physica Scripta](#) **95**, 045601 (2020).
- [59] V. Yakimenko, S. Meuren, F. Del Gaudio, C. Baumann, A. Fedotov, F. Fiuza, T. Grismayer, M. J. Hogan, A. Pukhov, L. O. Silva, and G. White, Prospect of studying nonperturbative qed with beam-beam collisions, [Phys. Rev. Lett.](#) **122**, 190404 (2019).
- [60] W. D. Kimura, H. M. Milchberg, P. Muggli, X. Li, and W. B. Mori, Hollow plasma channel

for positron plasma wakefield acceleration, [Phys. Rev. ST Accel. Beams](#) **14**, 041301 (2011).